Materials Chemistry and Physics 308 (2023) 128192

Contents lists available at ScienceDirect

Materials Chemistry and Physics

journal homepage: www.elsevier.com/locate/matchemphys

Selection on antimony-doped tin oxide (ATO) as an efficient support for iridium-based oxygen evolution reaction (OER) catalyst in acidic media

Inayat Ali Khan [a], Per Morgen [a], Saso Gyergyek [b], Raghunandan Sharma [a,*], Shuang Ma Andersen [a,**]

[a] Department of Green Technology, University of Southern Denmark, Odense, M 5230, Denmark
[b] Department for Materials Synthesis, Jozef Stefan Institute, Ljubljana, 1000, Slovenia

HIGHLIGHTS

- Fine Ir nanoparticles ~1.6 nm were successfully supported on ATOs using a polyol method.
- The synthesis conversion efficiency η_c is reported and compared among different ATOs.
- ATOs with lower surface O and high conductivity showed improved OER activity.
- Best supported Ir demonstrated 2.5 times activity that of commercial unsupported equivalent.

GRAPHICAL ABSTRACT

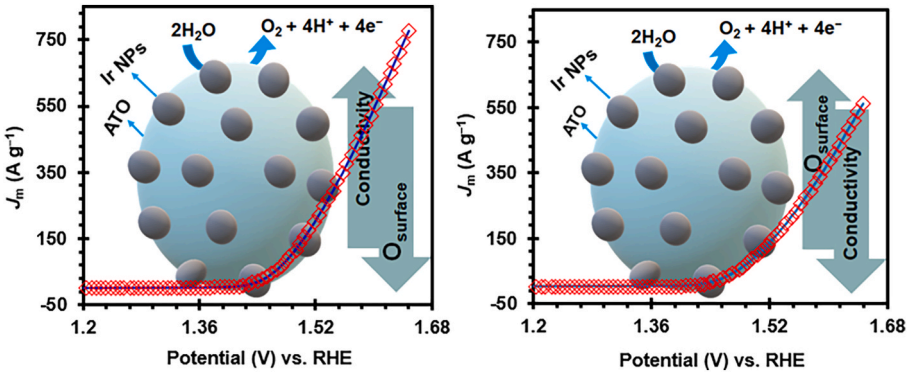

ARTICLE INFO

Keywords:
MW assisted polyol synthesis
Ir nanoparticles
Water splitting
Accelerated stress tests

ABSTRACT

Reducing the iridium content while preserving high OER activity is an important prerequisite for the progress of inexpensive anodic water splitting electrocatalysts in low pH medium. Here we report the effects of bulk and surface structures of antimony doped tin oxide (ATO) supports on the ATO supported Ir-based electrocatalyst's activity for oxygen evolution reaction (OER) in acidic media. Ability of the ATO supports to anchor the Ir nanoparticles, measured as the fraction of Ir species from reaction bath landed on ATO support (conversion efficiency; η_c), is found to be strongly dependent on its surface chemistry, characterized in terms of presence of surface oxygen groups ($O_{surface}$). Both $O_{surface}$ content and electronic conductivity of ATOs show strong influence on OER activity. In general, high conductivity and low $O_{surface}$ content are preferred for high OER activity, though low $O_{surface}$ may compromise η_c. The optimal catalyst demonstrates superior OER activity of 777 A g^{-1}, 2.5 times that of the state-of-the-art commercial catalyst at 1.65 V vs. RHE. Further, the synthesized catalysts exhibit durability comparable to that of the commercial counterpart.

* Corresponding author.
** Corresponding author.
E-mail addresses: rash@igt.sdu.dk (R. Sharma), mashu@igt.sdu.dk (S.M. Andersen).

https://doi.org/10.1016/j.matchemphys.2023.128192
Received 22 April 2023; Received in revised form 6 July 2023; Accepted 15 July 2023
Available online 17 July 2023
0254-0584/© 2023 The Authors. Published by Elsevier B.V. This is an open access article under the CC BY license (http://creativecommons.org/licenses/by/4.0/).

1. Introduction

Hydrogen is an attractive substitute to fossil fuels that permits sustainable energy supply without contributing to CO_2 emission [1]. With decreasing cost of green electricity, hydrogen generation *via* water splitting driven by photoenergy [2] or water electrolysis [3,4] is becoming highly relevant green fuel technology. Water electrolysis can be alkaline water electrolysis or polymer electrolyte membrane water electrolysis (PEMWE, acidic) with the latter having a few advantages such as, they are compact, withstand dynamic operating conditions, and can generate pressurized hydrogen and can operate at high current densities, compared to their alkaline counterparts [3]. In acid water electrolysis, while the cathodic reaction producing hydrogen is efficient, the anodic process, i.e., oxygen evolution reaction (OER), suffers from high overpotentials and sluggish reaction rate, therefore restraining the inclusive performance of electrolyzer [5–7]. Furthermore, severe OER conditions in acidic media limit the possible catalysts to noble metals (Ru and Ir), which are highly expensive and scarce [8]. Thus, lowering the noble metal content becomes an essential requirement for the practical implementation of acidic water electrolyzers [9].

Solutions to reduce the iridium (Ir) content have been intensively investigated, for example, partial replacement of Ir by a non-noble transition metal [10–13] and/or decrease of the size of the Ir crystallites to the nanometer scale [14,15]. However, the very oxidizing environment at PEMWE anodes (E > 2.0 V vs. RHE, presence of oxygen, acidic solution) renders common high-surface-area carbon supports unstable [16] and requires the development of alternatives. A class of such highly corrosion resistant catalyst supports is conductive metal oxides [17,18], for example, doped titanium, tin, or indium oxides [14–20]. Moreover, recent studies show that the presence of the metal/metal oxide support interactions can lead to improvement of the catalyst stability under OER conditions [21]. Amongst, antimony doped tin oxide (ATO) is found to be the most appropriate catalyst support due to its relatively high electronic conductivity, its stability under OER conditions in PEMWE, and its high surface area [22].

Controversially, recent studies have shown that ATO-based Ir electrocatalysts might not be efficient and long-term stable at high anodic potentials, which is ascribed to the leaching of antimony [23]. However, there are also many reports indicating high OER activity and stability of ATO-based Ir electrocatalysts. Oh et al., have reported Ir nanoparticles and nanodendrites (Ir-ND) on ATO which outperformed commercial Ir supported and unsupported catalysts in OER mass activity as well as in long-term stability for 15 h at constant current condition (10 mA cm^{-2}) [15,21]. Puthiyapura et al., reported the Adam fusion synthesis of IrO_2-based catalyst using commercial ATO support having conductivity of 4.3 × 10^{-3} S cm^{-1} and BET surface area up to 20–40 m^2 g^{-1}. The developed catalyst with >60 wt% Ir loading on ATO has presented improved OER activity, attributed to the high spreading of the IrO_2 nanoparticles (NPs) on the support surface. The ATO thermal stability up to 800 °C was reported however, the electrochemical stability of the Ir/ATO catalysts is not properly investigated [22]. In another investigation, Ohno et al., by using doped M − SnO_2 (M = Sb, Ta, and Nb) as the support for IrO_2 NPs, have shown that high conductivity of the support as well as catalyst is crucial factor for reaching high catalyst performance [24]. Similarly, Hartig-Weiss et al., have reported the polyol synthesis of Ir NPs on a high surface area (50 m^2 g^{-1}) and highly conductive ATO support (2 S cm^{-1}), and demonstrated their high OER activity. At 80 °C high temperature, the ATO supported catalyst also outperformed the commercial Ir-black and IrO_2/TiO_2 in terms of mass activity [25]. Mass activities ranging between 120 and 193 A g^{-1} at 1.6 V vs. RHE have been reported using high surface area ATO (165 m^2 g^{-1}) supported IrO_2 catalysts using Adam fusion method [26]. ATO (surface area up to 95 m^2 g^{-1}, conductivity of 0.02 S cm^{-1}) supported IrO_2 NPs synthesized through one-step organometallic chemical deposition have shown high mass activity, 7-fold higher than that of TiO_2 supported IrO_2. However, high Tafel slop was observed (63 mV dec^{-1}), attributed to the limited conductivity of ATO. Further, comparatively lower mass activity loss of 31% for IrO_2-ATO versus loss of 76% for IrO_2–TiO was observed in the stability test for 2 h at 1.6 V vs. RHE [27].

Numerous methods, including Adams fusion [28,29], pH-controlled hydrolysis [30,31], sole gel [32,33], polyol [34,35], *etc*. have been established to synthesize supported or unsupported Ir-based catalysts. Manganese oxide nanocomposites ($SrMnO_3$, $BaMnO_3$ and Zn_2MnO_4/ZnO) for OER have been studied by Salavati-Niasari and co-workers. The electrocatalysts were synthesized using sono-chemical method and factors such precursor, time and power of sonication affecting the particle size, morphology and structure have been thoroughly investigated. More uniform and homogenized nanostructures were identified as the best electrocatalysts for O_2 evolution [36–39]. During the past couple of decades, microwave (MW) technology for synthesis has been rapidly developed due to the exceptional properties of MWs that could spark interactions with chemical precursor and solvents to produce different results. Compared to conventional heating, the microwave-assisted heating accelerates the reaction rate, shortens the crystallization time, facilitates homogenous particles nucleation and can provide high conversion efficiency (η_c; fraction of the Ir species from reaction bath landed on the support in the desired form) with economical yield at industrial level [40,41]. Conventional polyol synthesis for Ir/ATO catalysts shows a η_c of around 60% [25], which can be improved to ~100% for MW-assisted synthesis [42].

Apart from parameters such as electronic conductivity and surface area, surface chemical state of the catalyst supports may play important role governing both the η_c during synthesis and the catalyst stability. However, this aspect has not been explored arguably for ATO supported Ir-based OER electrocatalysts. Furthermore, in supported catalysts, one of the important OER activity degradation mechanism could be high dissolution of the catalytic active species due to support corrosion. However, studies on ATO supported OER catalysts lack this important aspect.

In this study, we focus on some of the unexplored aspects of the ATO supported Ir-based OER catalysts by using different commercially available ATO supports. Surface chemistry modification of the ATO supports was achieved through acid-treatment [43]. High surface area and highly conducting pristine ATO samples, namely ATO1 and ATO2, along with their acid-treated counterparts ATO1.AT and ATO2.AT, were used as the catalyst supports. Effects of surface chemical states of the supports on the η_c, initial OER activity and stability of the synthesized electrocatalysts have been investigated.

2. Experimental

2.1. Chemicals

Metal precursor iridium (III) chloride hydrate ($IrCl_3.xH_2O$; Sigma-Aldrich), milliQ water (resistivity >18.2 MΩ cm), ethylene glycol (EG; anhydrous, 99.8%, Sigma-Aldrich), perchloric acid ($HClO_4$, 98%, Sigma-Aldrich) and hydrochloric acid (HCl, 37%; Sigma-Aldrich) for preparing the electrolyte and reaction bath were used without further treatments. ATO samples ATO1 (purity: 99.7%, particle size 5–15 nm, BET 54.5 m^2 g^{-1}, and conductivity 5 × 10^{-2}) and ATO2 (purity: 99.5%, particle size 20 nm, BET 56.7 m^2 g^{-1}, and conductivity 2.5 × 10^{-1}), supplied by Alroko®), were used as the catalyst supports.

2.2. Acid-treatment of ATO samples

Acid-treatment of the ATO powders was carried out to clean and activate the surface. The ATO1 and ATO2 (1000 mg) were separately mixed with 50 mL of HCl (37 wt%) and held at 65 °C for 1 h. The acid treated samples corresponding to ATO1 and ATO2, labeled respectively as ATO1.AT and ATO2.AT, were centrifuged and washed several times with ultrapure water until neutral pH and dried in a vacuum oven at 70 °C overnight.

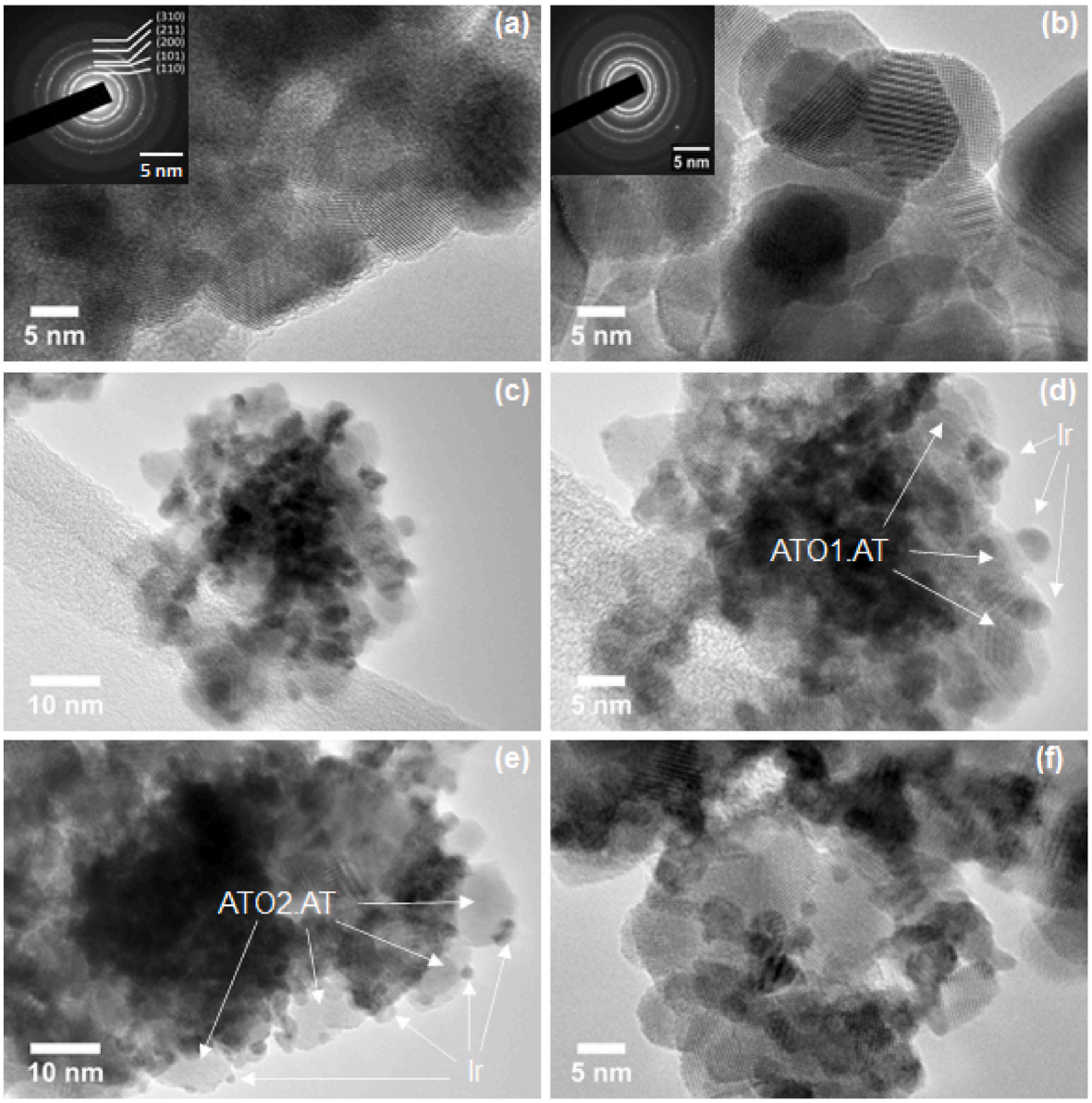

Fig. 1. TEM images of ATO1 (a) and ATO2 (b) (inset, SAED patterns-indexed according to tetragonal SnO_2, space group: $P4_2/mnm$). Low and high-resolution TEM images of Ir NPs supported on ATO1.AT (c, d) and Ir NPs supported on ATO2.AT (e, f).

2.3. Synthesis of the catalysts

The electrocatalysts were synthesized by utilizing a MW-assisted modified polyol synthesis method using a CEM Discovery SP® MW synthesizer. As an example, required amount of an ATO support (ATO1, ATO1.AT, ATO2 and ATO2.AT), corresponding to the Ir loading of 40 wt %, was dispersed in 20 mL of 5 mmol L^{-1} $IrCl_3.H_2O$ solution in an EG/ultrapure water mixture (7:3 *v/v*) through ultrasonication for 60 s at room temperature using a Hielscher UP200 St ultrasonic homogenizer. The ATO dispersed mixture was transferred to a 35 mL glass reactor and was exposed to MW-irradiation for 20 min at 140 °C. The MW synthesizer was operated in a dynamic power mode with a maximum power output of 200 W. After cooling, the samples were collected by centrifugation at 5000 rpm for 5 min, followed by washing with ultrapure water and drying overnight at 60 °C. XRF analyzer (Thermo Scientific Niton XL3t GOLDD+) was used for measuring the Ir content in the initial solution and in the final supernatant to estimate the reaction η_c [43].

2.4. Physical characterization

Rigaku Miniflex 600 X-ray diffractometer equipped with Cu Kα radiation ($\lambda = 1.5418$ Å) was used to obtain the X-ray diffraction (XRD) patterns of the catalysts, where a scan rate of 5° min^{-1} and a step size of 0.02° were used. SPECS® XPS instrument with a twin anode X-ray source and a hemispherical analyzer and Mg Kα (1253.6 eV) radiation was used for XPS analysis. The emitted photons were at 90° to the detector and adventitious carbon C 1*s* (284.7 eV) was used as an internal reference for energy calibration. CasaXPS software was used for spectra analysis, where Shirley type background correction and asymmetric Gaussian/Lorentzians (30% Lorentzian character) was adopted for peak fitting and deconvolution. The FWHM in the range of 0.7–2 eV was maintained for sub-peaks, keeping instrumental specific parameters.

Gas adsorption analysis was carried out using Micromeritics TriStar II analyzer. Prior to measurements, samples were degassed at 200 °C for 24 h under vacuum. A liquid nitrogen bath at 77 K was used for isotherm measurement. Bruner-Emmett-Teller (BET) model was used to calculate the surface area and the Barret-Joyner-Halenda (BJH) method was used

to calculate the pore size distribution. Finally, JEOL-JEM 2000 TEM transmission electron microscope (TEM) (thermionic source operated at 200 kV) was used to observe and analyze the bare ATO and Ir coated samples.

2.5. Electrochemical measurements

Electrochemical tests were performed using a three-electrode setup with the catalyst coated glassy carbon (GC) rotating disk electrode (RDE) as the working and a Pt wire as the counter electrode. Potentials were measured versus Ag/AgCl reference electrode (Aldrich; double junction; sat. KCl) and reported against reversible hydrogen electrode (RHE). The electrochemical measurements were carried out using a ZahnerIM6e electrochemical workstation. In a typical process, 10 mg of the catalyst was dispersed in 5 mL of a stock solution (1.84 vol% of 5 wt % Nafion, 20 vol% of isopropyl alcohol, and 78.2 vol% of ultrapure water) by ultrasonication for 60 s. Further, 10 μL of the ink was casted on GC RDE (diameter: 5 mm) and dried at 700 rpm. The Ir loading on the GC RDE was measured using XRF analyzer [43,44].

Prior to OER activity measurements, the electrode was activated in argon-saturated $HClO_4$ solution (0.1 mol L^{-1}) by potential cycling between 1.0 and 1.7 V (100 mV s^{-1}) for 20 cycles at 1600 rpm. The electrochemical impedance spectra were recorded in the frequency range from 1 kHz to 1 Hz at E_{over} = 270 mV vs. RHE. The OER measurements were carried out from 1.0 to 1.65 V at 10 mV s^{-1} sweep rate (2 cycles, 1600 rpm) and the data from the positive-going segment of the 2nd cycle was reported. The potential at the intersection points of the tangent at maximum slope of current was selected as the OER onset potential (E_{onset}) of a catalyst. Accelerated stress teste (AST) was carried out using cyclic voltammetry (CV) for 2000 cycles in the potential window from 1.0 to 1.7 V (100 mV s^{-1}) interrupted with intermediate observational cycling (2 cycles, 1–1.65 V, 10 mV s^{-1}) after specific stress cycle intervals.

3. Results and discussion

3.1. Conversion efficiency (η_c) and Ir loading

Compared to other platinum group metals, reduction of Iridium species during polyol synthesis to form Ir NPs is slow. As observed by the η_c calculated in terms of % decrease in the Ir concentration in the reaction bath due to formation of Ir/Ir-based NPs on the support surface, the η_c after long MW-irradiation (20 min) remains lower (60–80%) compared to that achieved for Pt in ~2.5 min MW-irradiation under similar synthesis environment (100%) [45].Moreover, the type of catalyst support affect the η_c significantly. In the present study, comparatively low reaction η_c values of ~74% and ~59% are observed for the Ir/ATO1 and Ir/ATO1.AT samples, while for Ir/ATO2 and Ir/ATO2.AT catalysts, the η_c values are ~98% and ~87%, respectively. The high η_c for ATO2 and ATO2.AT catalysts may be due to the appropriate interaction between the support surface active sites and the Ir NPs, facilitating deposition of the later. Comparatively low reaction conversion for acid treated *versus* pristine equivalent might be due to changed nature of the active sites on the support surface, as discussed later. Further, the observed lower than 100% η_c for polyol synthesis impacted the target Ir loading significantly. Instead of the target Ir loadings of 40 wt% Ir on the ATO supports, the obtained ones are found to be 30.0%, 24.0%, 39.2% and 35.0 wt%, respectively for the ATO1, ATO1.AT, ATO2, ATO2.AT supports.

3.2. Morphology and microstructure studies

It is well reported in the literature that there is a relationship between catalyst particle size and electrochemical activity [46]. With decreasing particle size the mass activity of the catalysts increases while the specific activity of the catalysts decreases. The critical size where

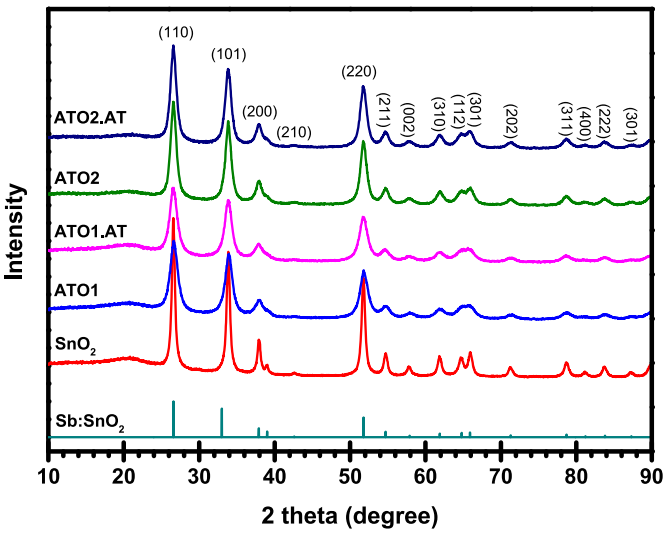

Fig. 2. PXRD patterns of the pristine and acid treated supports.

maximum catalytic activities might be obtained is in the range from 2 to 4 nm. Additionally, the choice of support materials for metal electrocatalysts was also found to greatly affect the catalytic activity through particles distribution and dispersion (surface area), particle adhesion and adsorption (determines the product yield and stability) and conductivity (reflecting the catalytic performance) [46]. These properties might lead to an enhanced catalytic activity with low metal loading which is significant for high priced materials.

Low- and high-resolution TEM analysis was carried out to investigate the structures and particle sizes of the commercial ATOs and Ir NPs deposited on ATOs. Fig. 1a, b and Fig. S1 show ATO NPs. They form agglomerates composed of well crystalline (Fig. 1a and b) nanoparticles. Individual nanoparticles are well resolved only at the edges of the agglomerates and are of size in the range from 5 to 10 nm. Selected area electron diffraction patterns (SAED) of ATO1 and ATO2 samples shows that in both cases sample consists of tetragonal SnO_2 NPs (insets in Fig. 1a and b). Ir NPs were deposited on ATO supports using the well-known MW-assisted polyol method. This method is common for reducing the noble metal precursors with ethylene glycol at the same time working as solvent, reducing agent, and stabilizer [47]. The high-resolution TEM images of Ir/ATO1.AT (Fig. 1c, d and Figs. S2a and b) display partial agglomerated Ir NPs present on the support surface. The aggregated particles are present as a separate bunch not properly intermingle within the support surface showing weak attachment of the metal NPs to the support sites. The partial adhesion of the Ir NPs to the ATO1.AT support also resulted in low reaction η_c of the MW-assisted polyol method at 140 °C. However, the TEM images of the as-prepared Ir/ATO2.AT catalysts-support couple (Fig. 1e and f and Fig. 2Sc, d), displaying small granular Ir NPs widely distributed on the support surface. The high-resolution TEM images of Ir/ATO2.AT (Fig. 1e and f) clearly shows that Ir NPs with a diameter of around 2 nm are well dispersed on the support surface. As the Ir NPs are mostly metallic (as confirmed by PXRD and XPS) and the electrochemical oxidation (activation) results in increase in particle size due to the formation of hydrous Ir oxide. These hydrous iridium oxides have particle size close to the desired values of around 4 nm which is significant for the excellent OER activities. Comparatively high reaction η_c of MW-assisted polyol method for Ir/ATO2.AT at 140 °C might be due the appropriate support surface sites for the strong attachment of metals NPs.

3.3. Bulk structure characterization

The structures of the pristine, acid treated supports and Ir NPs supported on ATO catalysts were characterized by PXRD measurements. In

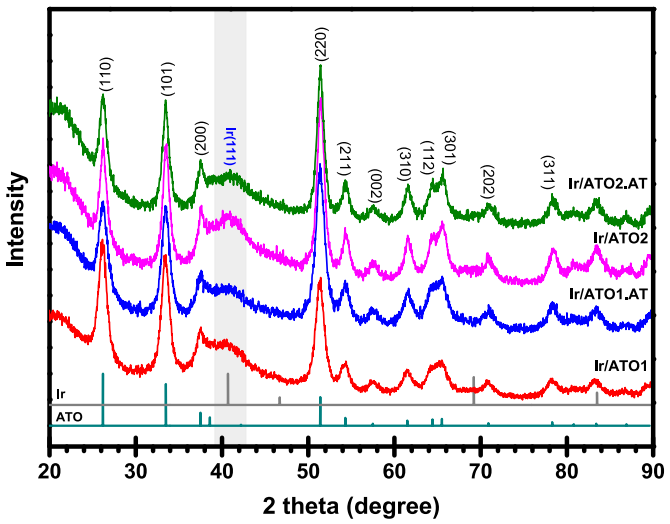

Fig. 3. PXRD patterns of a support and catalysts.

Fig. 2, the diffraction peaks at around $2\theta = 26.6°$, 33.9°, 37.9°, 42.6°, 51.8°, 54.7°, 57.8°, 62.0°, 64.8°, and 66.0° are index to the (110), (101), (200), (210), (220), (211), (002), (310), (112), and (301) planes of the tetragonal rutile-type SnO_2 structure (JCPDS: 21-1250) [48]. Antimony (Sb) is not readily identified in the PXRD, which might indicating Sb is within an intercalated structure under the host structure of SnO_2. Moreover, there is no significant difference on crystallinity among the four ATO samples. The diffraction peaks corresponding to the different planes of SnO_2 in the pristine ATOs are perfectly matching to that of SnO_2 in the acid treated ATOs, which indicates that acid treatment did not alter the bulk structure of the support.

Fig. 3 presents peaks for the SnO_2 at their respective 2θ values along with a broad peak at around 40.8° due to the (111) reflection plane of the *fcc* Ir metal [21] indicating the formation of Ir NPs supported on ATO (JCPDS: 87-0715). It is obvious from the X-ray diffraction studies that Ir content is metallic which indicates that the adopted method of synthesis is an effective means of converting precursors to the Ir NPs. No separate X-ray diffractions typical of tetragonal/rutile IrO_2 was detected. The Ir crystallite size ($D_{cryst.}$) was calculated using the following Scherrer equation (1):

$$D_{cryst.} = \frac{0.9\,\lambda}{\beta \cos\theta} \quad \cdots\cdots\cdots \quad (1)$$

where $D_{cryst.}$ is crystallite size (nm), λ is the X-ray wavelength (nm), β is the peak full width at half maximum (FWHM) and θ is the Bragg angel.

The crystallite size calculated for the Ir NP from $2\theta = 40.8°$ is around 1.6 nm for all catalysts which is in close agreement to the TEM analysis.

3.4. BET surface area analysis

The surface area and pore size distribution of the pristine and acid treated supports were measured by N_2 sorption experiments. The ATO supports exhibits a Type IV isotherm (Fig. 4) with negligible adsorbed volume at low relative pressure, hysteresis at medium relative and slight increase in the adsorbed volume at high relative pressure. This pattern of adsorption/desorption suggesting the absence of micropores and the presence of mesopores and macropores. The presence of mesopores and macropores in the ATOs matrix makes them ideal candidates to support metal NPs for better water molecules diffusion, mass transposition and enhanced OER activities. After acid treatment of the supports, no prominent change was observed in the N_2 adsorption volume which means that the porosity remained the same while the surfaces may be

Table 1
Surface parameters of the pristine and acid treated supports.

Supports	BET ($m^2\ g^{-1}$)	Pore volume ($m^3\ g^{-1}$)	Pore size (nm)
ATO1	54.5	0.10	6.5
ATO1.AT	56.7	0.11	6.5
ATO2	56.7	0.10	10.0
ATO2.AT	56.2	0.10	10.0

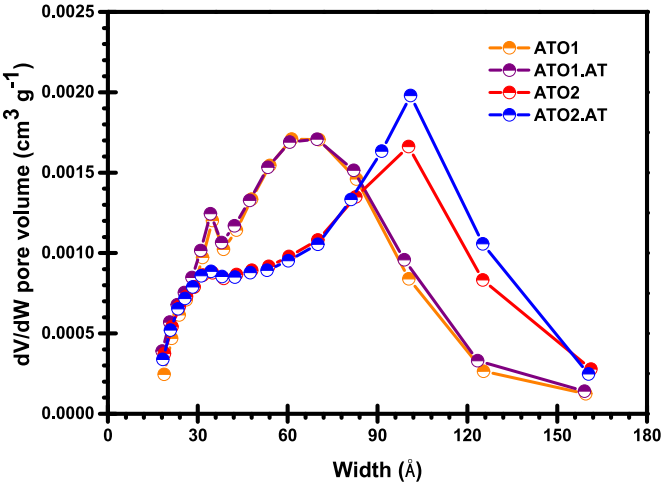

Fig. 5. Pore size distribution plots of pristine and acid treated ATOs.

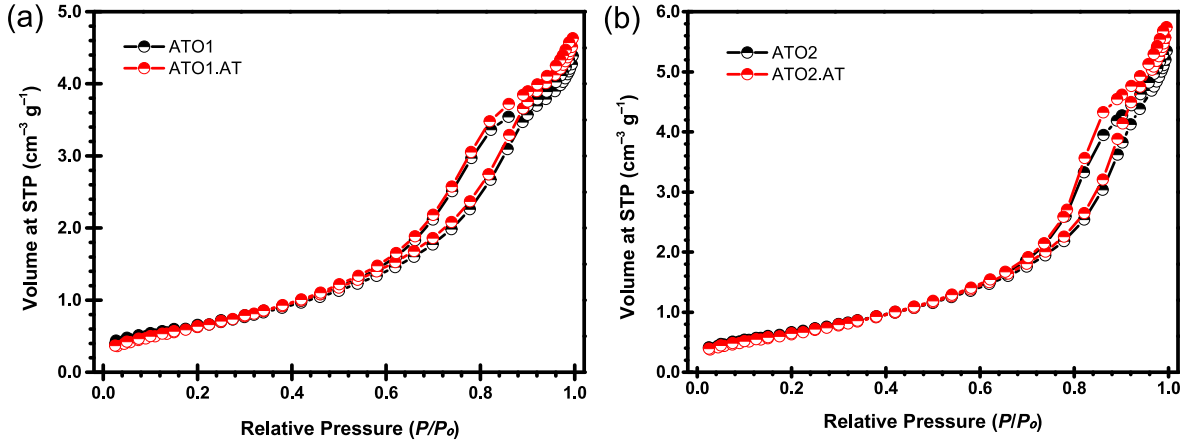

Fig. 4. N_2 adsorption/desorption isotherms of pristine and acid treated ATO1 (a) and ATO2 (b).

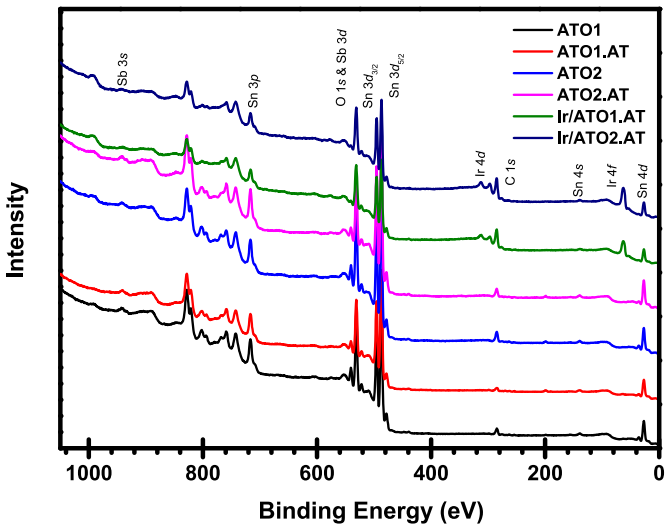

Fig. 6. XPS survey spectra of pristine and acid treated supports and synthesized catalysts.

Table 2
Elemental contents from XPS survey.

Supports and Catalysts	Atoms (%)			
	O	Sn	Sb	Ir
ATO1	69.9 ± 0.22	22.8 ± 0.26	7.3 ± 0.23	–
ATO1.AT	68.2 ± 0.12	24.7 ± 0.14	7.1 ± 0.11	–
ATO2	70.4 ± 0.23	22.3 ± 0.28	7.4 ± 0.24	–
ATO2.AT	66.7 ± 0.52	26.4 ± 0.55	7.0 ± 0.51	–
Ir/ATO1.AT	66.7 ± 0.42	19.2 ± 0.43	7.0 ± 0.41	7.1 ± 0.40
Ir/ATO2.AT	64.7 ± 0.17	20.2 ± 0.14	6.8 ± 0.15	8.3 ± 0.16

activated for particles adhesion and effective catalysis. The recorded BET surface areas and porosities are given in Table 1. The pore size distribution plots of ATO1/ATO1.AT and ATO2/ATO2.AT have maxima at around 6.5 and 10 nm, respectively (Fig. 5). As a comparison the pore maxima is shifted to higher values in case of ATO2/ATO2.AT support which reveals comparatively more open mesopores for gas diffusion and mass transport.

3.5. Surface chemical structure and band diagram

The elemental composition and electronic states of the elements in support and in catalysts were determined by XPS analysis [21,25,49–54]. In Fig. 6, the survey XPS spectra show obvious signals of O, Sn, Sb and Ir in the supports and in the catalysts (Table 2). The XPS results clearly shows that there is not a big difference between the metals content of the supports before and after acid treatment which indicates negligible change in the bulk composition upon acid-treatment. However, the oxygen content of the supports was decreased upon acid treatment, which is advantageous for the electronic conductivity of the catalyst. The C peak in all spectra is caused by adventitious carbon in the environment.

High resolution XPS fitting was carried out to further investigate the oxidation states and their relative percent composition. Table 3 shows the binding energies and relative percent amount of the different transition levels for the main atoms detected in the samples. Special attention has been paid to the analysis of the chemical state of the Sb atom in the surface. Figs. S3(a and c), Figs. S4(a and c) and Fig. 7a, c shows the XPS spectra obtained between 524 and 546 eV for the supports and the catalysts in which peaks corresponding to transitions of Sb and O atoms can be observed. The peak corresponding to the Sb $3d_{5/2}$ spin orbit component is completely covered by the peak of the O 1*s* transition. This peak can be separated from the O 1*s* peak by making use of the Sb $3d_{3/2}$ component at higher binding energy with spin-orbit separation of 9.3 eV [49,55]. The peak of Sb $3d_{3/2}$ is centered in the range from 540.2 to 540.4 eV in bare supports, Table 2. These binding energies corresponds to Sb^{5+}, therefore no Sb^{3+} was detected on the surface [49]. The XPS peak position of Sb $3d_{3/2}$ remain the same (Table 3) when the ATO1.AT and ATO2.AT supports were loaded with iridium which means no electron transfer from Sb to Ir and vice versa. The constant electronic state of Sb in supports is advantageous for the long-term stability of the catalyst. It has been reported that the electronic interaction between Sb and Ir lead to leakage of Sb from the support and overall deactivation of the catalyst [42]. In the O 1*s* transition, a peak centered at around 531 eV (Table 3) is related with oxygen directly bonded to a metal atom and characteristic of metallic oxides (M − O). The high-resolution Sn 3*d* spectra for bare supports (Figure 7, Figure 3Sb, d and Fig. 4Sb, d) consists of two asymmetric peaks at around 487.1 eV and 495.5 eV which are respectively assigned to Sn^{4+} $3d_{5/2}$ and $3d_{3/2}$ spin-orbit splitting showing SnO_2. No clear discrimination between SnO and SnO_2 or hydroxylated species was observed [49]. However, comparing to the bare supports negligibly small shift toward low binding energies was observed in the peak positions of Sb and Sn while small shift toward high binding energy was observed in the peak position of O for catalysts, Table 3. Such a small change in binding energies might be due to (*i*) interaction between Ir NPs and support and/or (*ii*) partial reduction of the support surface during polyol synthesis. Furthermore, compared to the bare supports, the percent area corresponding to O 1*s* increased while that of Sb^{5+} decreased for catalysts due to more oxygen contribution from the surface oxides in Ir NPs.

The high resolution Ir 4*f* spectra (Fig. 7c, f) for supported catalysts show $4f_{7/2}$ and $4f_{5/2}$ spin-orbit doublet, appearing at different energies which confirm that the as-synthesized catalysts have Ir^0 and Ir^{4+}; the latter may correspond to the IrO_2 or $Ir(OH)_4$. The peaks presenting metallic Ir appeared at 60.9 and 63.9 eV for the supported catalysts [25,42,52,53], Table 3. Jang *at el.* have investigated the phenomenon of strong metal-support interaction (SMSI) between Ir and ATO support at different temperatures (100, 120, 140, 160, 180 and 200 °C) using microwave-assisted polyol synthesis- [42]. In their XPS investigation, the Sb^{5+} in support was reduced to Sb^{3+} (negative shift in BEs) and

Table 3
XPS fits binding energies and components atomic concentrations.

Samples	ATO1		ATO2		ATO1.AT		ATO2.AT		Ir/ATO1.AT-24%		Ir/ATO2.AT-35%	
Peaks	BE (eV)	Area (%)	BE (eV)	Area (%)	BE (eV)	Area (%)	BE (eV)	Area (%)	BE (eV)	Area (%)	BE (eV)	Area (%)
O 1*s*	531.1	63	531.1	60	531.1	66	531.1	69	531.4	92	531.3	93
Sb^{5+} $3d_{5/2}$	531.1	22	531.0	24	531.0	21	531.1	19	530.9	05	531.0	05
Sb^{5+} $3d_{3/2}$	540.4	15	540.3	16	540.2	14	540.4	12	540.2	03	540.3	03
Sn^{4+} $3d_{5/2}$	487.1	60	487.1	60	487.0	60	487.1	60	487.0	60	487.0	60
Sn^{4+} $3d_{3/2}$	495.5	40	495.6	40	495.5	40	495.5	40	495.5	40	495.4	40
Ir^0 $4f_{7/2}$	–	–	–	–	–	–	–	–	60.9	47	60.9	47
Ir^0 $4f_{5/2}$	–	–	–	–	–	–	–	–	63.9	35	63.9	35
Ir^{4+} $4f_{7/2}$	–	–	–	–	–	–	–	–	62.8	10	62.9	11
Ir^{4+} $4f_{5/2}$	–	–	–	–	–	–	–	–	65.8	08	65.9	08

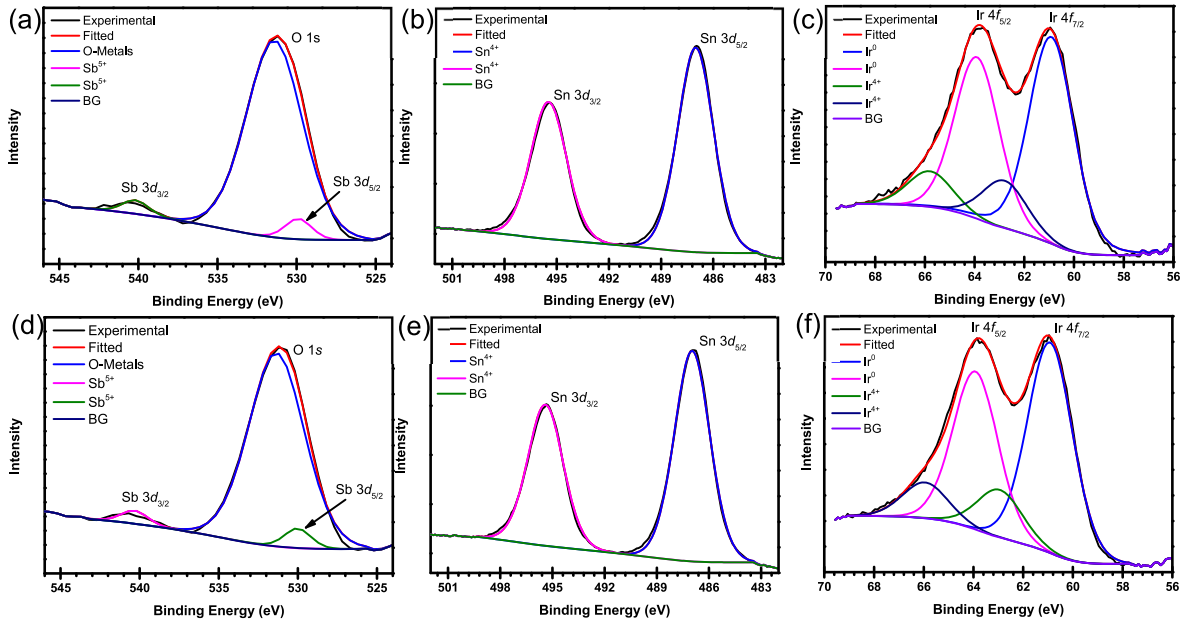

Fig. 7. High resolution XPS spectra of O 1*s*, Sb 3*d*, Sn 3*d* and Ir 4*f* for Ir/ATO1.AT (a–d) and Ir/ATO2.AT (d–f).

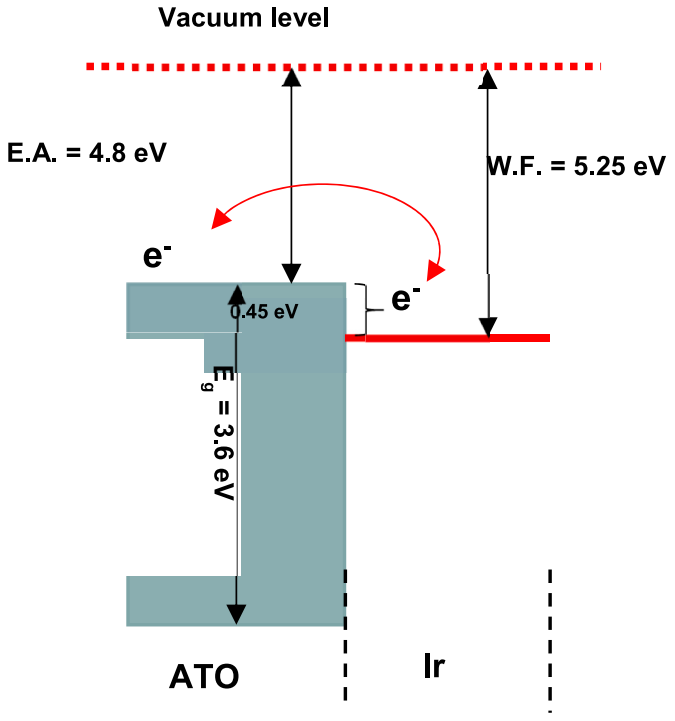

Fig. 8. Energy band diagram of the Ir and ATO.

precursor iridium was partially reduced to Ir^{1+} when the reaction was carried out at 100/120 °C and the respective catalysts showed comparatively weak OER activities. However, when the catalysts were prepared at onset temperature of 140 °C the binding energies of Sb 3*d* and Sn 3*d* showed a positive shift which is an indication of SMSI. Herein this study, we performed details XPS investigation of two commercial supports (ATO1 and ATO2) and their acid-treated counterparts (ATO1. AT and ATO2.AT) to find out SMSI at the interface of Ir-support while the Ir NPs were deposited at onset temperature of 140 °C using MW-assisted polyol synthesis. The high resolution XPS analysis showed that the surface interaction and electron transfer between support and Ir is negligible and showed weak SMSI when the catalyst were prepared at 140 °C. The Ir NPs are only surface deposited showing good initial OER performance, but worse long-term stability. This means that 140 °C is the optimum temperature to reduce Ir precursor to metallic Ir NPs and deposit on support but cannot initiate and promote SMSI. The absence of SMSI at the junction of Ir-ATO can be explained by the reduction mechanism of ethylene glycol. The work by Jang et al. [42] also shows that the reduction power of ethylene glycol increases with increasing temperature. This means that high reaction temperature (≈150–160 °C) [47] is needed to reduce the Ir precursor as well to initial and promote the phenomenon of SMSI. Thus, to find out a correlation between temperature and SMSI is our future line of investigation to produce quality OER catalysts.

Table 3 shows the detailed information obtained from peak fitting, indicating that the catalysts with 24 and 35 wt% Ir loading have similar Ir^0 to Ir^{4+} ratios. The atomic percentage of Ir:IrO_x in the Ir NPs was found to be 82:18 for both the ATO1.AT and ATO2.AT supported catalysts. This means that a metallic Ir core (bulk 82%) is always covered by a layer (18% in total) of IrO_2 or $Ir(OH)_2$ [25].

ATO is a n-type semiconductor that is suitable to generate extra electrons *via* oxygen vacancies [56] and this property allow to use ATO ceramic as a catalyst support for OER. When Ir NPs were deposited on ATO support, transfer of electrons at the junction of Ir/ATO is facilitated due to the relatively low energy barrier around 0.45 eV between Ir (work function of Ir = 5.25 eV) and ATO (electron affinity of ATO = 4.8 eV), as can be seen in Fig. 8. The exchange of electrons is highly important for the high catalytic activity and stability of the Ir/ATO catalysts. However, such transfer of electrons (metal-support interaction) has not been observed in the XPS binding energy shift.

3.6. Initial OER activity

The OER catalytic activities of the synthesized catalysts were examined in $HClO_4$ solution using CV RDE setup at room temperature. The catalysts can be arranged in the decreasing order of their E_{onset} (Table S1) as; Ir/ATO1> Ir/ATO1.AT ≈ Ir/ATO2≈ IrO_2 AA > Ir/ATO2. AT. It is evident that the Ir/ATO2.AT catalyst significantly outperformed the commercial IrO_2 and other homemade catalysts in the whole potential window. Specifically, the overpotential of Ir/ATO2.AT catalyst to reach current density of 10 mA cm^{-2} is 330 mV similar to that of

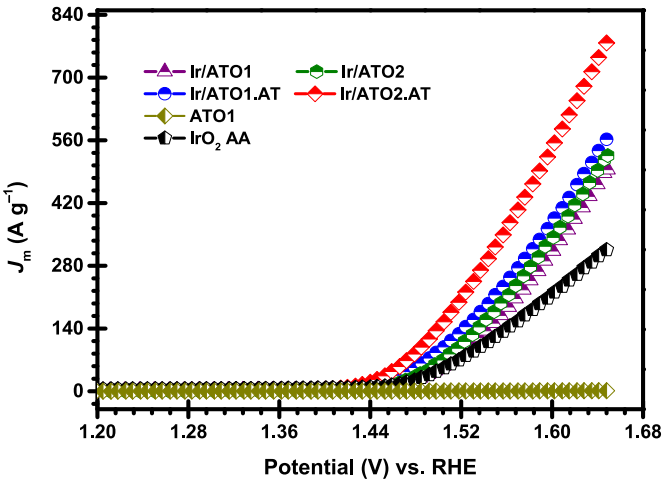

Fig. 9. Mass specific activities of the catalysts. The potential window was from 1 to 1.65 V, the scan rate was 10 mV s^{-1} using $HClO_4$ as electrolyte (pH = 1).

Table 4
Over potentials and mass-specific activities of the synthesized and literature reported electrocatalysts.

Catalysts	Ir load (wt.%)	E_{over} (V)	J_m (A g^{-1})	Ref.
Ir-ND/ATO	–	280	69.8 at 1.51 V	[15]
IrO_x/ATO	20	280	39.1 at 1.51 V	[21]
Ir/ATO	11	–	185 at 1.5 V	[25]
IrO_x/ITO-B	11	–	207 at 1.525 V	[57]
IrO_2/ATO	9.4	–	70 at 1.525 V	[27]
Ir/ATO (180 °C)	20	–	153 at 1.51 V	[42]
IrO_x/ATO	20	280	≈98 at 1.51 V	[50]
$IrNiO_x$/Meso-ATO-*T*	19.3	–	90 at 1.51 V	[58]
Nb–TiO_2/IrO_2	8	–	654 at 1.7 V	[59]
IrO_x/ATO	20	–	41.3 at 1.55 V	[60]
Ir_{NP}-ITO	4.1	–	10 at 1.47 V	[61]
Ir/ATO1.AT	24	360	562 at 1.65 V	This work
Ir/ATO2.AT	35	330	777 at 1.65 V	This work

commercial IrO_2 and around 30 mV lower than other as-synthesized catalysts. The excellent performance of Ir/ATO2.AT catalyst can be attributed to the high dispersion of active metals NPs on acid-treated support and well active catalytic sites. The specific activities at 1.50 V (current normalized with electrode geometric surface area, J_{geo}) indicate that Ir/ATO2.AT catalyst almost surpass the other counterparts and commercial IrO_2 (Table S1) and the catalysts order of decreasing their specific activities is Ir/ATO2.AT > IrO_2 AA > Ir/ATO1.AT > Ir/ATO2 > Ir/ATO1. The enhanced activity of Ir/ATO2.AT correspond to structure modulation of Ir NPs by the addition of acid-treated support (ATO2.AT). However, it should be noted that the specific activity of Ir/ATO2 (2.30 mA cm^{-2}) is higher than that of Ir/ATO1 (1.57 mA cm^{-2}), which is mainly due to the high conductivity of ATO2 (2.5×10^{-1} S cm^{-1}) in contrast to ATO1 (5×10^{-2} S cm^{-1}).

The mass activities of all the bare supports and catalysts were calculated and shown in Fig. 9, Fig. S5and Table S1, which clearly demonstrate the superiority of the synthesized catalysts over commercial IrO_2. Bare supports showed negligible mass specific OER activity, Fig. S5. The mass specific activity of Ir/ATO2.AT at 1.65 V emerges as the best one with 777 A g^{-1}, which is 2.5 times that of commercial IrO_2. The high resistivity support (ATO1) catalyst, Ir/ATO1, have also much better mass activity than commercial IrO_2. Obviously, the pristine ATOs and the acid treated ATOs have effectively enhanced the catalytic efficiency by promoting particles dispersion, mass transport and effective catalytic sites. The high OER mass activities of the as-synthesized catalysts over commercial IrO_2 are assigned to the considerable increase in the hydrous Ir oxide active surface area because of the use of small Ir NPs. Besides increase in the active surface area, the high dispersion of the Ir NPs on high surface area and conductive ATO supports, make use of the OER active sites at maximum, might further improve the OER activity. The electrochemical impedance spectroscopic (EIS) measurements were carried out for representative bare support (ATO2.AT) and representative catalyst (Ir/ATO2.AT) and the Nyquist plots are shown in Fig. S6. The electrolyte resistance (R_e), indicated by the high frequency intersection point on the real axis, is shifted to lower value for the electrocatalyst (2.4 Ω) in comparison to the bare support (22 Ω) implies on electrolyte concentration change as a results of water oxidation. The catalyst exhibits small semicircle showing fast electron transfer (low charge transfer resistance; R_{ct} = 23.6 Ω), high conductivity and fast reaction kinetics which corresponds to the high OER activity.

For comparison, the composition and electrochemical performances of literature reported ceramic oxides supported Ir-based electrocatalysts are tabulated in Table 4. Oh et al. have reported iridium nanoparticles and nanodendrites (Ir-ND) supported on ATO for OER with mass-specific activities of 98 A g^{-1} and 69.8 A g^{-1} at 1.51 V vs. RHE along with good constant-current stability. The electrocatalytic activity and long-term stability was attributed to the metal/metal-oxide support interaction and corrosion stable conductive oxide support. Hartig-Weiss et al. have reported electrocatalyst compose of highly dispersed 2 nm Ir nanoparticles on ATO (2 S cm^{-1}) with 11 wt% total Ir load which is screen for OER activity in acidic media. The catalyst has exhibited 185 A g^{-1} mass-specific activity at 1.5 V vs RHE [25]. Mohamed and coworkers have reported a metal-organic chemical deposition method for accommodating IrO_x on two different supports. The catalyst with 9.4 wt% Ir load on ATO has demonstrated mass-specific activity up to 70 A g^{-1} while the catalyst with 11 wt% Ir load on ITO has demonstrated mass-specific activity up to 207 A g^{-1} at 1.525 V vs RHE. The high catalytic activity of IrO_x/ITO was attributed to the nanoparticle's coverage effect, and low interparticle distances that were also promoted the long-term stability of the catalyst [27,57]. Catalysts compose of IrO_x and ATO support having 20 wt% Ir loading been reported by Jang et al. which was synthesized by MW-assisted polyol method. Strong metal-support interaction was considered as a catalyst stability deteriorating factor and the catalyst obtained at 180 °C presented mass-specific activity as high as 153 A g^{-1} at 1.51 V vs RHE [42]. Ir load up to 20 wt% on ATO is also reported by Claudel et al. with mass-specific activity of 39.1 A g^{-1} at 1.51 V vs RHE. Low OER activity of the catalyst is assigned to the progressive increase of the Ir oxidation state along with increased concentration of hydroxyl group and water molecules [50]. Nong et al., have reported $IrNi_x$@IrO_x core-shell deposited on mesoporous-ATO having Ir load of 19.3% with mass-specific OER value of 90 A g^{-1} at 280 mV vs. RHE overpotential [58]. Niobium-doped titanium oxide (NTO) with high conductivity (440 S cm^{-1}) was deposited with 1 nm thin layer of IrO_2 using atomic layer deposition method. The thin film electrocatalyst with Ir load of 8 wt% presented OER activity of 654 A g^{-1} at an overpotential of 460 mV vs. RHE [59]. Antimony-doped tin oxide (ATO) having conductivity up to 0.11 S cm^{-1} is reported by Cherevko and coworkers for the 20 wt% Ir load OER electrocatalyst. The electrocatalyst IrO_x/ATO have shown mass-specific OER activity up to 41.3 A g^{-1} at 1.55 V vs. RHE and 50% loss in stability after 1000 AST cycles. Mass specific activity up to 10 A g^{-1} at 1.47 V vs. RHE was achieved by 4.1 wt% Ir load on indium tin oxide (ITO) support which was attributed to the Ir small size (1.5 nm) and oxo-hydroxide structure [61]. In current studies, our catalysts showed significantly high mass activity of 777 A g^{-1} at 1.65 V and a slightly higher overpotential of 330 mV vs RHE.

3.7. Catalyst stability

While achieving high OER activity is important, good stability may play an even more important role in practical water-splitting applications [62]. The degradation behavior of the catalysts was evaluated using the AST protocol [60,63], for 2000 CV cycles and the results were compared with that of commercial IrO_2. In AST experiments, the

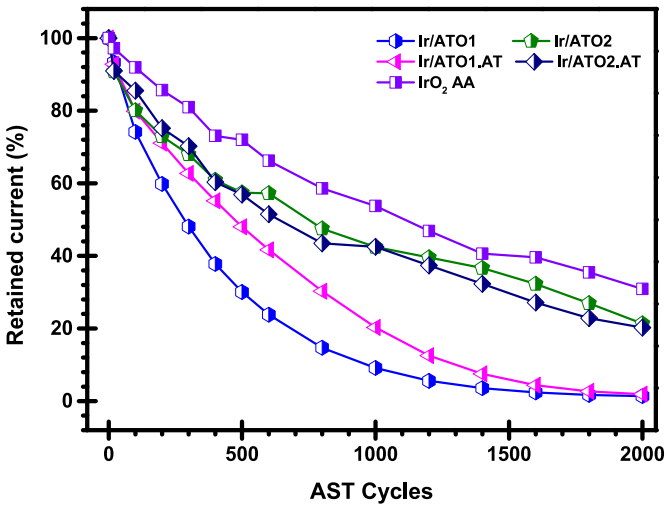

Fig. 10. AST performances of the studied catalysts. The potential window was from 1 to 1.65 V, the scan rate was 10 mV s^{-1} using $HClO_4$ as electrolyte (pH = 1).

Table 5
Post AST J_m, retained current, and Ir weight loss after 2000 cycles.

Catalysts	Post AST J_m (A g^{-1})	Ret. Current (%)	Ir weight loss (%)
Ir/ATO1	7	1.4	15.4
Ir/ATO1.AT	11	1.9	13.9
Ir/ATO2	112	21.4	3.9
Ir/ATO2.AT	157	20.3	4.0
IrO_2 AA	94	30.9	4.1

working electrode with catalysts layer was subjected to 2000 cycles between 1 and 1.7 V at scan rate of 100 mV s^{-1}. The OER measurements were performed (1–1.65 V, 10 mV s^{-1}) before potential cycling and after the specific number of potential cycling to observe the difference in the performance. It can be seen in Fig. 10 that the percent retained current is gradually decreasing with increasing number of AST cycles. The Ir/ATO2 and Ir/ATO2.AT catalysts electrodes retained about 21% of its initial current, while the Ir/ATO1 and Ir/ATO1.AT catalysts electrodes have about 2% of their initial current over the 2000 AST cycles. Low AST performances corresponding to Ir/ATO1 and Ir/ATO1.AT *versus* Ir/ATO2 and Ir/ATO2.AT can be assign to the support properties effect as ATO1/ATO1.AT have low Ir content (30 and 24%) resulted in overall lower conductivity and high Ir poising in acidic media. Moreover, in comparison to commercial IrO_2 all the as-synthesized catalysts have demonstrated low AST stability might be due to the absence of metal-support interaction and low conductivity, not enough for long term catalyst exposure to the electrochemical water oxidation. Such low AST performances for the supported catalysts have also been reported by Cherevko and co-workers [60].

The XRF analysis was carried out to investigate the Ir weight loss before and after AST measurements. On average about 15% of the initial weight of Ir was lost for Ir/ATO1 and Ir/ATO1.AT catalysts and only 4% of the initial weight of Ir was lost for Ir/ATO2 and Ir/ATO2.AT catalysts during AST (Table 5). High Ir loss for the ATO1/ATO1.AT-based catalysts show comparatively weak surface interaction of the Ir NPs to the support surface. AST measurements were also carried out for bare supports to investigate the support stability (Sn). The XRF results before and after AST (Fig. 11) show no prominent change in the peak intensity and peak position for Sn in all the supports which means that the total quantity and electronic state of SnO_2 remained the same over the 2000 AST cycles. This means that the decrease in percent retained current of the catalysts with increasing AST is due to the Ir NPs detachment and

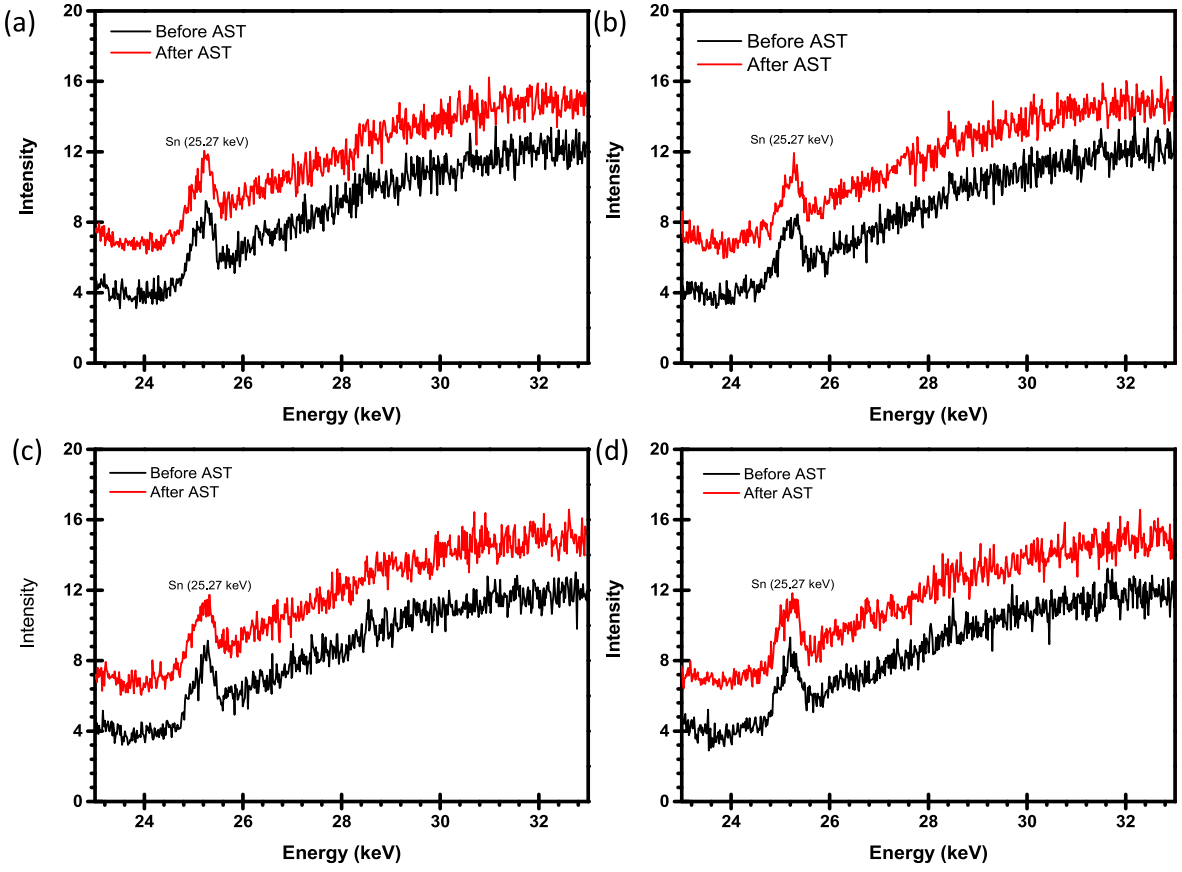

Fig. 11. Selected region XRF spectra before and after AST (a) ATO1, (b) ATO1.AT, (c) ATO2 and (d) ATO2.AT.

degradation in acidic environment that is more severe for ATO1/ATO1.AT supported catalysts.

4. Conclusions

In conclusion, MW-assisted highly efficient polyol synthesis method was developed to prepare ATO supported catalysts for OER. Based on iridium precursor conversion, the reaction η_c values of 98% and 87% were achieved for ATO2 and ATO2.AT supported catalysts, and the combinations were superior OER catalysts than the ATO1/ATO1.AT supported or commercial counterparts. The high initial OER activity of the synthesized catalysts was assigned to the Ir NPs high dispersion on support surface and high conductivity. However, the long-term stability is compromised due to negligible observed metal-support electron interaction. The catalysts were arranged in the decreasing order of their mass specific activities as; Ir/ATO2.AT (777 A g^{-1}) > Ir/ATO1.AT (562 A g^{-1}) > Ir/ATO2 (526 A g^{-1}) > Ir/ATO1 (494 A g^{-1}) > IrO_2 AA (305 A g^{-1}). Among the synthesized catalysts, the Ir/ATO2.AT catalyst have demonstrated high stability during 2000 AST cycles experiment and retained about 21% of its initial current density. Essentially, both η_c values and OER performance of an ATO supported catalyst are found to be affected significantly by the surface functionality of the ATO. The study will facilitate the selection of promising catalyst supports for prospective development of the supported OER catalysts.

CRediT author statement

Inayat Ali Khan: Validation, Soft-ware, Formal analysis, Investigation, Visualization, Writing - original draft. Per Morgen: Methodology, Investigation, Writing - review & editing. Saso Gyergyek: Methodology, Investigation, Writing - review & editing. Raghunandan Sharma: Conceptualization, Methodology, Writing - review & editing, Supervision, Project administration. Shuang Ma Andersen: Conceptualization, Methodology, Writing - review & editing, Supervision, Project administration, Funding acquisition.

Declaration of competing interest

The authors guarantee that none of the material presented here has been published or is under consideration for publication elsewhere and declare no interest of conflict.

Data availability

Data will be made available on request.

Acknowledgments

The authors acknowledge financial support from Innovation Fund Denmark, InnoExplorer program, Nr. 9122-00112; Danish Agency for Higher Education and Science, ESS lighthouse on hard materials in 3D, SOLID, Grant number 8144-00002B; Energi Fyns udviklingsfond and Slovenian Research Agency (research core funding Nos. P2-0089). The authors thank Dr. Swapnil Sanjay Karade for his technical assistance, department technician Rikke Klindt Muller for performing the BET surface area measurements, and the Centre of Excellence in Nanoscience and Nanotechnology – Nanocenter for the use of Transmission Electron Microscope Jeol JEM-2100.

Appendix A. Supplementary data

Supplementary data to this article can be found online at https://doi.org/10.1016/j.matchemphys.2023.128192.

References

[1] G.H. Rau, H.D. Willauer, Z.J. Ren, The global potential for converting renewable electricity to negative-CO_2-emissions hydrogen, Nat. Clim. Change 8 (2018) 621–625.
[2] Y. Tachibana, L. Vayssieres, J.R. Durrant, Artificial photosynthesis for solar water-splitting, Nat. Photonics 6 (2012) 511–518.
[3] A. Ursua, L.M. Gandia, P. Sanchis, Hydrogen production from water electrolysis: current status and future trends, Proc. IEEE 100 (2012) 410–426.
[4] Z.W. Seh, J. Kibsgaard, C.F. Dickens, I. Chorkendorff, J.K. Nørskov, T.F. Jaramillo, Combining theory and experiment in electrocatalysis: insights into materials design, Science 355 (2017), eaad4998.
[5] N.-T. Suen, S.-F. Hung, Q. Quan, N. Zhang, Y.-J. Xu, H.M. Chen, Electrocatalysis for the oxygen evolution reaction: recent development and future perspectives, Chem. Soc. Rev. 46 (2017) 337–365.
[6] C. Spöri, J.T.H. Kwan, A. Bonakdarpour, D.P. Wilkinson, P. Strasser, The stability challenges of oxygen evolving catalysts: towards a common fundamental understanding and mitigation of catalyst degradation, Angew. Chem. Int. Ed. 56 (2017) 5994–6021.
[7] T. Reier, H.N. Nong, D. Teschner, R. Schlögl, P. Strasser, Electrocatalytic oxygen evolution reaction in acidic environments–reaction mechanisms and catalysts, Adv. Energy Mater. 7 (2017), 1601275.
[8] C.C.L. McCrory, S. Jung, J.C. Peters, T.F. Jaramillo, Benchmarking heterogeneous electrocatalysts for the oxygen evolution reaction, J. Am. Chem. Soc. 135 (2013) 16977–16987.
[9] U. Babic, M. Suermann, F.N. Büchi, L. Gubler, T.J. Schmidt, Critical review-identifying critical gaps for polymer electrolyte water electrolysis development, J. Electrochem. Soc. 164 (2017) F387.
[10] L.A. da Silva, V.A. Alves, M.A.P. da Silva, S. Trasatti, J.F.C. Boodts, Oxygen evolution in acid solution on IrO_2+TiO_2 ceramic films. A study by impedance, voltammetry and SEM, Electrochim, Acta 42 (1997) 271–281.
[11] G. Chen, X. Chen, P.L. Yue, Electrochemical behavior of novel Ti/IrO_x−Sb_2O_5−SnO_2 anodes, J. Phys. Chem. B 106 (2002) 4364–4369.
[12] T. Reier, Z. Pawolek, S. Cherevko, M. Bruns, T. Jones, D. Teschner, S. Selve, A. Bergmann, H.N. Nong, R. Schlögl, K.J.J. Mayrhofer, P. Strasser, Molecular insight in structure and activity of highly efficient, low-ir ir–ni oxide catalysts for electrochemical water splitting (OER), J. Am. Chem. Soc. 137 (2015) 13031–13040.
[13] N.J. Pérez-Viramontes, I.L. Escalante-García, C. Guzmán-Martínez, M. Galván-Valencia, S.M. Durón-Torres, Electrochemical study of Ir–Sn–Sb–O materials as catalyst-supports for the oxygen evolution reaction, J. Appl. Electrochem. 45 (2015) 1165–1173.
[14] T. Reier, M. Oezaslan, P. Strasser, Electrocatalytic oxygen evolution reaction (OER) on Ru, Ir, and Pt catalysts: a comparative study of nanoparticles and bulk materials, ACS Catal. 2 (2012) 1765–1772.
[15] H.-S. Oh, H.N. Nong, T. Reier, M. Gliech, P. Strasser, Oxide-supported Ir nanodendrites with high activity and durability for the oxygen evolution reaction in acid PEM water electrolyzers, Chem. Sci. 6 (2015) 3321–3328.
[16] K. Kinoshita, Carbon: Electrochemical and Physicochemical Properties, John Wiley & Sons, New York, 1988.
[17] V. Ávila-Vázquez, J. Cruz, M. Galván-Valencia, J. Ledesma-García, L. Arriaga, C. Guzmán, S. Durón-Torres, Electrochemical study of Sb-doped SnO_2 supports on the oxygen evolution reaction: effect of synthesis annealing time, Int. J. Electrochem. Sci. 8 (2013) 10586–10600.
[18] R.E. Fuentes, J. Farell, J.W. Weidner, Multimetallic electrocatalysts of Pt, Ru, and Ir supported on anatase and rutile TiO_2 for oxygen evolution in an acid environment, Electrochem. Solid State Lett. 14 (2011) E5.
[19] E. Oakton, D. Lebedev, M. Povia, D.F. Abbott, E. Fabbri, A. Fedorov, M. Nachtegaal, C. Copéret, T.J. Schmidt, IrO_2-TiO_2: a high-surface-area, active, and stable electrocatalyst for the oxygen evolution reaction, ACS Catal. 7 (2017) 2346–2352.
[20] Y.-J. Wang, D.P. Wilkinson, J.J.C.r. Zhang, Noncarbon support materials for polymer electrolyte membrane fuel cell electrocatalysts, Chem. Rev. 111 (2011) 7625–7651.
[21] H.-S. Oh, H.N. Nong, T. Reier, A. Bergmann, M. Gliech, J. Ferreira de Araújo, E. Willinger, R. Schlögl, D. Teschner, P. Strasser, Electrochemical catalyst–support effects and their stabilizing role for IrO_x nanoparticle catalysts during the oxygen evolution reaction, J. Am. Chem. Soc. 138 (2016) 12552–12563.
[22] V.K. Puthiyapura, M. Mamlouk, S. Pasupathi, B.G. Pollet, K. Scott, Physical and electrochemical evaluation of ATO supported IrO_2 catalyst for proton exchange membrane water electrolyser, J. Power Sources 269 (2014) 451–460.
[23] S. Geiger, O. Kasian, A.M. Mingers, K.J. Mayrhofer, S. Cherevko, Stability limits of tin-based electrocatalyst supports, Sci. Rep. 7 (2017) 1–7.
[24] H. Ohno, S. Nohara, K. Kakinuma, M. Uchida, H. Uchida, Effect of electronic conductivities of iridium oxide/doped SnO_2 oxygen-evolving catalysts on the polarization properties in proton exchange membrane water electrolysis, Catalyst 9 (2019) 74.
[25] A. Hartig-Weiss, M. Miller, H. Beyer, A. Schmitt, A. Siebel, A.T.S. Freiberg, H. A. Gasteiger, H.A. El-Sayed, Iridium oxide catalyst supported on antimony-doped tin oxide for high oxygen evolution reaction activity in acidic media, ACS Appl. Nano Mater. 3 (2020) 2185–2196.
[26] S.-B. Han, Y.-H. Mo, Y.-S. Lee, S.-G. Lee, D.-H. Park, K.-W. Park, Mesoporous iridium oxide/Sb-doped SnO2 nanostructured electrodes for polymer electrolyte membrane water electrolysis, Int. J. Hydrogen Energy 45 (2020) 1409–1416.
[27] Z.S. Rajan, T. Binninger, P.J. Kooyman, D. Susac, R. Mohamed, Technology, Organometallic chemical deposition of crystalline iridium oxide nanoparticles on

antimony-doped tin oxide support with high-performance for the oxygen evolution reaction, Catal. Sci. Technol. 10 (2020) 3938–3948.
[28] J. Xu, G. Liu, J. Li, X. Wang, The electrocatalytic properties of an IrO_2/SnO_2 catalyst using SnO_2 as a support and an assisting reagent for the oxygen evolution reaction, Electrochim. Acta 59 (2012) 105–112.
[29] E. Mayousse, F. Maillard, F. Fouda-Onana, O. Sicardy, N. Guillet, Synthesis and characterization of electrocatalysts for the oxygen evolution in PEM water electrolysis, Int. J. Hydrogen Energy 36 (2011) 10474–10481.
[30] A. Skulimowska, M. Dupont, M. Zaton, S. Sunde, L. Merlo, D.J. Jones, J. Rozière, Proton exchange membrane water electrolysis with short-side-chain Aquivion® membrane and IrO_2 anode catalyst, Int. J. Hydrogen Energy 39 (2014) 6307–6316.
[31] I.A. Lervik, M. Tsypkin, L.-E. Owe, S. Sunde, Electronic structure vs. electrocatalytic activity of iridium oxide, J. Electroanal. Chem. 645 (2010) 135–142.
[32] S. Ardizzone, C.L. Bianchi, L. Borgese, G. Cappelletti, C. Locatelli, A. Minguzzi, S. Rondinini, A. Vertova, P.C. Ricci, C. Cannas, Physico-chemical characterization of IrO_2–SnO_2 sol-gel nanopowders for electrochemical applications, J. Appl. Electrochem. 39 (2009) 2093–2105.
[33] Y. Murakami, S. Tsuchiya, K. Yahikozawa, Y. Takasu, Preparation of ultrafine IrO_2-Ta_2O_5 binary oxide particles by a sol-gel process, Electrochim. Acta 39 (1994) 651–654.
[34] M.S. Thomassen, T. Mokkelbost, E. Sheridan, A. Lind, Supported nanostructured Ir and IrRu electrocatalysts for oxygen evolution in PEM electrolysers, ECS Trans. 35 (2011) 271.
[35] A. Marshall, B. Børresen, G. Hagen, M. Tsypkin, R. Tunold, Preparation and characterisation of nanocrystalline $IrxSn_{1-x}O_2$ electrocatalytic powders, Mater. Chem. Phys. 94 (2005) 226–232.
[36] S. Gholamrezaei, M. Salavati-Niasari, Sonochemical synthesis of $SrMnO_3$ nanoparticles as an efficient and new catalyst for O_2 evolution from water splitting reaction, Ultrason. Sonochem. 40 (2018) 651–663.
[37] S. Gholamrezaei, M. Amiri, O. Amiri, M. Salavati-Niasari, H. Moayedi, Ultrasound-accelerated synthesis of uniform $SrMnO_3$ nanoparticles as water-oxidizing catalysts for water splitting systems, Ultrason. Sonochem. 62 (2020), 104899.
[38] X.-X. Tian, S. Gholamrezaei, O. Amiri, M. Ghanbari, A. Dashtbozorg, M. Salavati-Niasari, Zn_2MnO_4/ZnO nanocomposites: one step sonochemical fabrication and demonstration as a novel catalyst in water splitting reaction, Ceram. Int. 46 (2020) 25789–25801.
[39] S. Gholamrezaei, M. Ghanbari, O. Amiri, M. Salavati-Niasari, L.K. Foong, $BaMnO_3$ nanostructures: simple ultrasonic fabrication and novel catalytic agent toward oxygen evolution of water splitting reaction, Ultrason. Sonochem. 61 (2020), 104829.
[40] C.O. Kappe, A. Stadler, D. Dallinger, Microwaves in Organic and Medicinal Chemistry, John Wiley & Sons, 2012.
[41] Y. Asakuma, S. Matsumura, A. Saptoro, Method for suppressing superheating behavior during microwave assisted nanoparticle formation by ethylene glycol addition, Chem. Eng. Process: Process Intensif. 132 (2018) 11–15.
[42] H. Jang, J.-H. Lee, J.R. Lee, T.-W. Kim, Metal–support interaction can deactivate IrO_x/Sb:SnO_2 OER catalysts in polyol process, ACS Appl. Energy Mater. 5 (2022) 9297–9302.
[43] S.S. Karade, R. Sharma, S. Gyergyek, P. Morgen, S.M. Andersen, IrO_2/Ir composite nanoparticles (IrO_2@Ir) supported on TiN_xO_y coated TiN: efficient and robust oxygen evolution reaction catalyst for water electrolysis, ChemCatChem 15 (2023), e202201470.
[44] M. Chourashiya, R. Sharma, S.M. Andersen, Accurate determination of catalyst loading on glassy carbon disk and its impact on thin film rotating disk electrode for oxygen reduction reaction, Anal. Chem. 90 (2018) 14181–14187.
[45] R. Sharma, Y. Wang, F. Li, J. Chamier, S.M. Andersen, Synthesis of a Pt/C electrocatalyst from a user-friendly Pt precursor (ammonium hexachloroplatinate) through microwave-assisted polyol synthesis, ACS Appl. Energy Mater. 2 (2019) 6875–6882.
[46] B.E. Hayden, Particle size and support effects in electrocatalysis, Acc. Chem. Res. 46 (2013) 1858–1866.
[47] C. Bock, C. Paquet, M. Couillard, G.A. Botton, B.R. MacDougall, Size-selected synthesis of PtRu nano-catalysts: reaction and size control mechanism, J. Am. Chem. Soc. 126 (2004) 8028–8037.
[48] H.S. Chin, K.Y. Cheong, K.A. Razak, Review on oxides of antimony nanoparticles: synthesis, properties, and applications, J. Mater. Sci. 45 (2010) 5993–6008.
[49] F. Montilla, E. Morallón, A. De Battisti, S. Barison, S. Daolio, J. Vazquez, Preparation and characterization of antimony-doped tin dioxide electrodes. 3. XPS and SIMS characterization, J. Phys. Chem. B 108 (2004) 15976–15981.
[50] F. Claudel, L. Dubau, G. Berthomé, L. Sola-Hernandez, C. Beauger, L. Piccolo, F. Maillard, Degradation mechanisms of oxygen evolution reaction electrocatalysts: a combined identical-location transmission electron microscopy and X-ray photoelectron spectroscopy study, ACS Catal. 9 (2019) 4688–4698.
[51] H.P. Tran, H.N. Nong, H.-S. Oh, M. Klingenhof, M. Kroschel, B. Paul, J. Hübner, D. Teschner, P. Strasser, Catalyst–support surface charge effects on structure and activity of IrNi-based oxygen evolution reaction catalysts deposited on tin-oxide supports, Chem. Mater. 34 (2022) 9350–9363.
[52] V.A. Saveleva, L. Wang, O. Kasian, M. Batuk, J. Hadermann, J.J. Gallet, F. Bournel, N. Alonso-Vante, G. Ozouf, C. Beauger, K.J.J. Mayrhofer, S. Cherevko, A.S. Gago, K.A. Friedrich, S. Zafeiratos, E.R. Savinova, Insight into the mechanisms of high activity and stability of iridium supported on antimony-doped tin oxide aerogel for anodes of proton exchange membrane water electrolyzers, ACS Catal. 10 (2020) 2508–2516.
[53] C. J.F, J. Moulder, R.C. King, Handbook of X-Ray Photoelectron Spectroscopy: A Reference Book of Standard Spectra for Identification and Interpretation of XPS Data, 1995.
[54] R. Sharma, M.A. Karlsen, P. Morgen, J. Chamier, D.B. Ravnsbæk, S.M. Andersen, Crystalline disorder, surface chemistry, and their effects on the oxygen evolution reaction (OER) activity of mass-produced nanostructured iridium oxides, ACS Appl. Energy Mater. 4 (2021) 2552–2562.
[55] Z. Deng, D. Chen, F. Tang, J. Ren, A.J. Muscat, Synthesis and purple-blue emission of antimony trioxide single-crystalline nanobelts with elliptical cross section, Nano Res. 2 (2009) 151–160.
[56] M. Utriainen, K. Kovács, J. Campbell, L. Niinistö, F. Réti, Controlled electrical conductivity in SnO_2 thin films by oxygen or hydrocarbon assisted atomic layer epitaxy, J. Electrochem. Soc. 146 (1999) 189.
[57] J.-A. Hoffman, Z.S.H.S. Rajan, D. Susac, M.C. Matoetoe, R. Mohamed, Influence of support physicochemical properties on the oxygen evolution reaction performance of ITO-supported IrO_x nanoparticles, J. Phys. Chem. C 127 (2023) 894–906.
[58] H.N. Nong, H.S. Oh, T. Reier, E. Willinger, M.G. Willinger, V. Petkov, D. Teschner, P. Strasser, Oxide-supported $IrNiO_x$ core–shell particles as efficient, cost-effective, and stable catalysts for electrochemical water splitting, Angew. Chem. Int. Ed. 54 (2015) 2975–2979.
[59] A.G. Hufnagel, S. Häringer, M. Beetz, B. Böller, D. Fattakhova-Rohlfing, T. Bein, Carbon-templated conductive oxide supports for oxygen evolution catalysis, Nanoscale 11 (2019) 14285–14293.
[60] G.C. da Silva, S.I. Venturini, S. Zhang, M. Löffler, C. Scheu, K.J. Mayrhofer, E. A. Ticianelli, S. Cherevko, Oxygen evolution reaction on tin oxides supported iridium catalysts: do we need dopants? Chemelectrochem 7 (2020) 2330–2339.
[61] D. Lebedev, C. Copéret, Small, narrowly distributed iridium nanoparticles supported on indium tin oxide for efficient anodic water oxidation, ACS Appl. Energy Mater. 2 (2018) 196–200.
[62] F.-Y. Chen, Z.-Y. Wu, Z. Adler, H. Wang, Stability challenges of electrocatalytic oxygen evolution reaction: from mechanistic understanding to reactor design, Joule 5 (2021) 1704–1731.
[63] R. Badam, M. Hara, H.-H. Huang, M. Yoshimura, Synthesis and electrochemical analysis of novel IrO_2 nanoparticle catalysts supported on carbon nanotube for oxygen evolution reaction, Int. J. Hydrogen Energy 43 (2018) 18095–18104.